Virus-templated Pt–Ni(OH)$_2$ nanonetworks for enhanced electrocatalytic reduction of water

Virus-Templated Pt–Ni(OH)$_2$ Nanonetworks for Enhanced Electrocatalytic Reduction of Water

William C. Records [a, f, †], Youngmin Yoon [b, †], Jacqueline F. Ohmura [c, f], Nicolas Chanut [e], Angela M. Belcher [c, d, f, *]

Departments of [a] Chemical Engineering, [b] Chemistry, [c] Biological Engineering, [d] Materials Science and Engineering, Massachusetts Institute of Technology, 77 Massachusetts Avenue, Cambridge, MA 02139, United States

[e] MultiScale Materials Science for Energy and Environment (<MSE>^{2}), MIT-CNRS Joint Laboratory / MIT Energy Initiative, Massachusetts Institute of Technology, Cambridge, MA 02139, United States

[f] Koch Institute for Integrative Cancer Research, Massachusetts Institute of Technology, 500 Main Street, Cambridge, MA 02139, United States

[†] These authors contributed equally

Corresponding Author

* E-mail: belcher@mit.edu

Abstract

Clean hydrogen production *via* water electrolysis is incumbent upon the development of high-performing hydrogen evolution reaction electrocatalysts. Despite decades of commercial maturity, however, alkaline water electrolyzers continue to suffer from limitations in electrocatalytic activity and stability, even with noble metal catalysts. In recent years, combining platinum with oxophilic materials, such as metal hydroxides, has shown great promise for improving performance potentially by enabling stronger water dissociation at the surface of electrocatalysts. In this work, we leveraged the nanoscopic proportions and surface programmability of the filamentous M13 bacteriophage in the design, synthesis, and exceptional performance of 3D nanostructured biotemplated electrocatalysts for alkaline hydrogen evolution. We developed a facile synthesis method for phage-templated, Pt–$Ni(OH)_2$ nanonetworks, relying on scalable techniques like electroless deposition and air oxidation. After optimization of the platinum content, our materials display –4.9 A mg^{-1}_{Pt} at –70 mV versus the reversible hydrogen electrode, the highest reported mass activity in 1 M KOH to date, and undergo minimal changes in overpotential under galvanostatic operation at –10 mA cm^{-2}_{geo}. Looking forward, the performance of these catalysts suggests that biotemplating nanostructures with M13 bacteriophage offers an interesting new route for developing high-performing electrocatalysts.

Keywords: hydrogen evolution reaction; electrocatalysis; M13 bacteriophage; 3D nanostructure; biotemplating

1. Introduction

Hydrogen has stimulated intensive research focus over the last several decades as an alternative to fossil fuels due to its high gravimetric energy density and carbon-free combustion [1–3]. Nevertheless, its production remains dominated by environmentally unfriendly methods, including steam methane reforming and coal gasification [4,5]. Water electrolysis offers the possibility to couple hydrogen production with more environmentally friendly methods, especially when used in conjunction with renewably generated electricity. Despite its maturity, water electrolysis accounts for only 4% of the global hydrogen production today due to its relatively high capital costs and uncertainty regarding future costs and performance [6], both of which could be mitigated by improving electrocatalysts.

Several strategies are currently being explored to engineer more cost-effective performance in water-splitting electrocatalysts. Efforts to minimize the utilization of noble metals or to find suitable, earth-abundant alternatives are among the most active areas of research [7]. Water splitting is comprised of two half reactions, the cathodic hydrogen evolution reaction (HER) and the anodic oxygen evolution reaction (OER), both of which require electrocatalysts to occur with minimal overpotentials. The OER is generally understood as easier to catalyze under alkaline conditions with both precious and non-precious materials. Moreover, as high OER overpotentials dominate electrolyzer inefficiencies, it tends to direct the electrolyte choice on a commercial scale [8,9]. Although a number of potential HER electrocatalysts have approached the performance of platinum benchmarks in acid electrolyte, including metal chalcogenides, phosphides, nitrides, and carbides [10–14], this success has not been mirrored in alkaline electrolyte. Materials typically feature 2–3 times lower activity in alkaline HER than in acidic HER, due to mechanistic changes which have not been fully elucidated [15]. It is commonly understood that the adsorption energy of hydrogen is the defining material descriptor correlated with high HER activity. Due to the scarcity of hydronium, the proton donor in typical acidic electrolytes, dissociative adsorption of water dominates the proton-donating mechanistic step in alkaline HER. Strong alkaline HER electrocatalysts, then, must feature both strong dissociative water adsorption and optimal hydrogen adsorption [16].

Following from these two design criteria, several recent reports have concluded that cooperative, bimetallic electrocatalysts can greatly improve alkaline HER activity. In particular, the incorporation of an oxophilic material with traditionally active materials results in enhanced electrocatalytic performance. Previous works suggest that oxophilic sites strongly adsorb water molecules, which can then dissociate into adsorbed hydrogen atoms and recombine into molecular hydrogen on the neighboring active surface [17]. Pt–$Ni(OH)_2$ in particular has shown promise, as $Ni(OH)_2$ displays a strong affinity toward water adsorption, and platinum is well-known for its high HER activity. Most reported Pt–$Ni(OH)_2$ electrocatalysts in literature, however, have been prepared by modifying single-crystal platinum catalysts with $Ni(OH)_2$ ad-islands [18] or similar, nanostructured materials [19–22]. These examples have been tested with a mechanistic study in mind, rather than developing a more cost-efficient, practical material that minimizes the utilization of platinum. If Pt–$Ni(OH)_2$ materials are to be implemented in commercial alkaline water electrolyzer cathodes, in which transition metal electrocatalysts like Ni–Mo alloys are used [23], further optimization of the platinum loading is necessary, as well as the development of specific design principles.

One heretofore unexplored method of water-splitting electrocatalyst design is to use biological templates to nucleate and control the growth of electrocatalytic materials. Biotemplating is characterized by several inherent advantages not found in traditionally inorganic synthesis methods. Under mild conditions, biological organisms can form a range of complex nano and microstructures that are typically difficult to synthesize, including nanowires, nanoplatelets, and nanofoams [24]. Additionally, organisms like the filamentous M13 bacteriophage offer a genetic handle on material-binding properties, thereby offering simultaneous control over surface chemistry, nanostructure, and microstructure. Phage has already been successfully incorporated into a number of energy applications, including photovoltaics [25,26], Na–ion and Li–ion batteries [27–29], and piezoelectric energy generation [30]. In the design of higher-performing alkaline HER electrocatalysts, biotemplating with phage facilitates the formation of high-surface-area, contiguous nanostructures and the ability to assemble multiple components, such as Pt and $Ni(OH)_2$, at the nano and microscale.

Herein, we report the design, synthesis, and exceptional performance of 3D, biotemplated Pt–$Ni(OH)_2$ nanonetworks in alkaline HER electrocatalysis. We leveraged the nanoscopic proportions and surface programmability of the M13 bacteriophage to further the traditionally nonbiological field of material design. Electrocatalysts were prepared using facile, binder-free techniques, including electroless deposition and air oxidation, directly on conductive substrates. The Pt–$Ni(OH)_2$ nanonetworks possess high activity, –200 mA cm^{-2}_{geo} and –4.9 A mg^{-1}_{Pt} at –70 mV versus the reversible hydrogen electrode (RHE), and outperform commercial Pt/C, phage-templated Pt nanonetworks, and phage-templated Ni nanonetworks in alkaline media. With optimized platinum loading, the Pt–$Ni(OH)_2$ nanonetworks demonstrate the highest mass activities in 1 M KOH reported to date. They show stable performance, undergoing far smaller changes in overpotential than platinum controls over four hours of passing a current density of –10 mA cm^{-2}_{geo}. Finally, several insights related to material design were obtained; most notably, the cooperativity between Pt and $Ni(OH)_2$ may suffer from lower efficiency at higher platinum loadings due to poorer dispersion and a diminution of accessible, electrocatalytically active sites.

2. Experimental Section

In this work, we designed Pt–$Ni(OH)_2$ nanonetworks using M13, a filamentous bacteriophage 880 nm long and 8 nm in diameter, as a material building block. Phage-templating was selected as it enables the fabrication of high-surface-area catalysts while maintaining high surface site accessibility [31]. Additionally, the surface coat proteins of phage provide a genetic handle to control surface chemistry. We leveraged previously reported, phage-templated, nickel nanofoams to control the nano and microscale morphology of Pt–$Ni(OH)_2$ electrocatalysts. The synthesis process is summarized in **Figure 1** and is detailed more completely in Section S1.3 in the Supporting Materials. In order to bind positively charged metal cations and facilitate metallization, we utilized the phage clone EEAE. This clone is engineered to display the negatively charged sequence E–E–A–E on the N–terminus of the main coat protein, pVIII. Solutions of phage particles were first assembled into hydrogels under the cross-linking action of glutaraldehyde on a conductive, titanium substrate. Next, electroless deposition (ELD) with sodium

hypophosphite as the reducing agent was utilized to directly coat nickel onto the phage scaffold. The shell of the nanonetworks was then fabricated upon exposing the metallized nanostructures to dilute chloroplatinic acid, before rinsing and drying. The aerobic, aqueous conditions of incubating this solution encouraged the formation of a thin $Ni(OH)_2$ sheath, as well as the galvanic deposition of platinum nanoislands [32]. Macroscopically, the resulting Pt–$Ni(OH)_2$ "nanonetworks" appeared as thin films with geometric surface areas ranging between 0.2 and 0.3 cm^2.

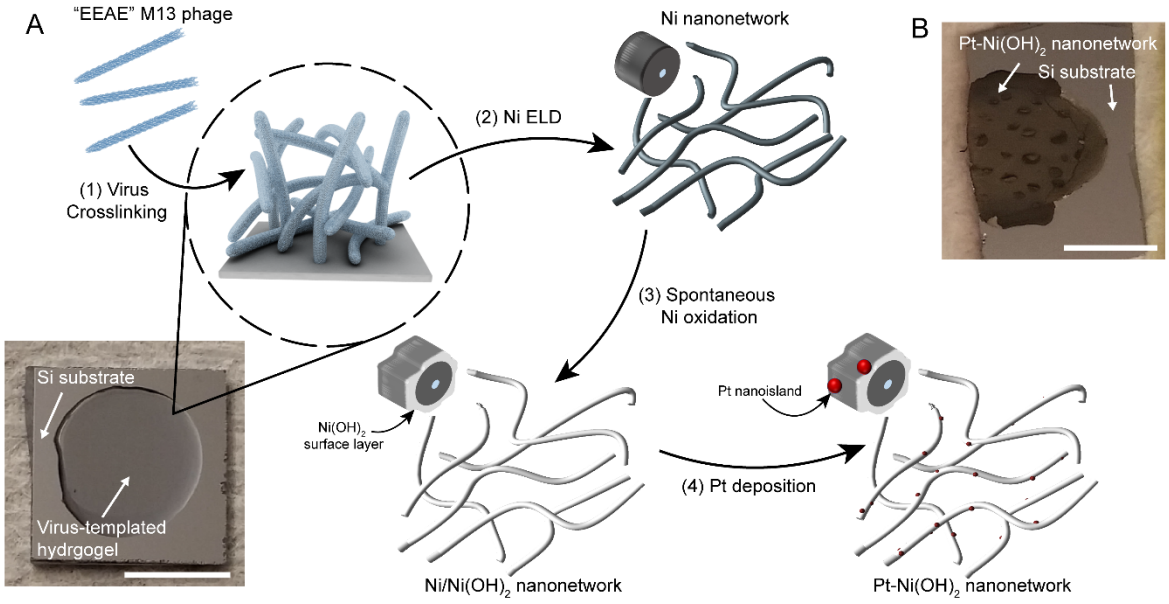

Figure 1. (a) Synthesis of Pt–$Ni(OH)_2$ nanonetworks: EEAE M13 virus particles are (1) crosslinked and (2) metallized. (3) Nickel spontaneously oxidizes to $Ni(OH)_2$ in aerobic conditions, and (4) platinum is deposited on the surface of the phage-templated scaffold. (b) Macroscopic view of a Pt–$Ni(OH)_2$ nanonetwork. Scale bars in (a) and (b) are 5 mm.

The performance of Pt–$Ni(OH)_2$ nanonetworks as HER electrocatalysts in alkaline electrolyte was assessed using standard benchmarking electrochemical tests. Cyclic voltammetry and chronoamperometry were conducted in a typical three-electrode setup in order to quantify the overall activity and perform a Tafel analysis, respectively. Activity was normalized by either the geometric area or mass of platinum in the sample. As platinum is far more active than nickel in HER electrocatalysis, the mass of platinum was chosen as a suitable approximation for the number of active sites. Chronopotentiometric and chronoamperometric stability testing and H_2 product measurement was conducted using a glass H-cell

setup and anion exchange membrane to prevent gas crossover. A more detailed description of the testing setup and methodology can be found in Sections S1.7–S1.9 in the Supplementary Materials.

3. Results and Discussion

3.1 Physical Characterization

Transmission electron microscope (TEM) and scanning electron microscope (SEM) images of the Pt–$Ni(OH)_2$ nanonetworks are given in **Figure 2a–c**. The structures are characterized by interconnected, biotemplated, metallized nanowires, decorated with platinum nanoislands typically on the order of 200 nm, as dictated by the templated nanowire diameter (200 nm). A nanoisland size dependence on the platinum precursor concentration was observed, where larger nanoislands (>200 nm) formed at higher platinum concentrations. Phosphorus was also co-deposited with nickel during ELD, originating from the use of sodium hypophosphite as the nickel reducing agent. The choice of sodium hypophosphite was intentional, as (1) it enables nickel deposition under buffered, neutral conditions, and (2) it does not have enough reducing power to reduce platinum under these conditions [33]. This prevented undesirable platinum ELD in subsequent synthesis steps. The composition of nanofoams at different nickel deposition times was probed using ICP–OES and reported in **Figure S1a–d**. The increase in mass of both nickel and phosphorus is relatively steady with time during the first 90 minutes of deposition, indicating a constant deposition rate. Conversely, the relative elemental composition first changes rapidly and then stabilizes between 10 and 11 wt% phosphorus after 40 minutes. Both behaviors are typical of hypophosphite ELD baths [34].

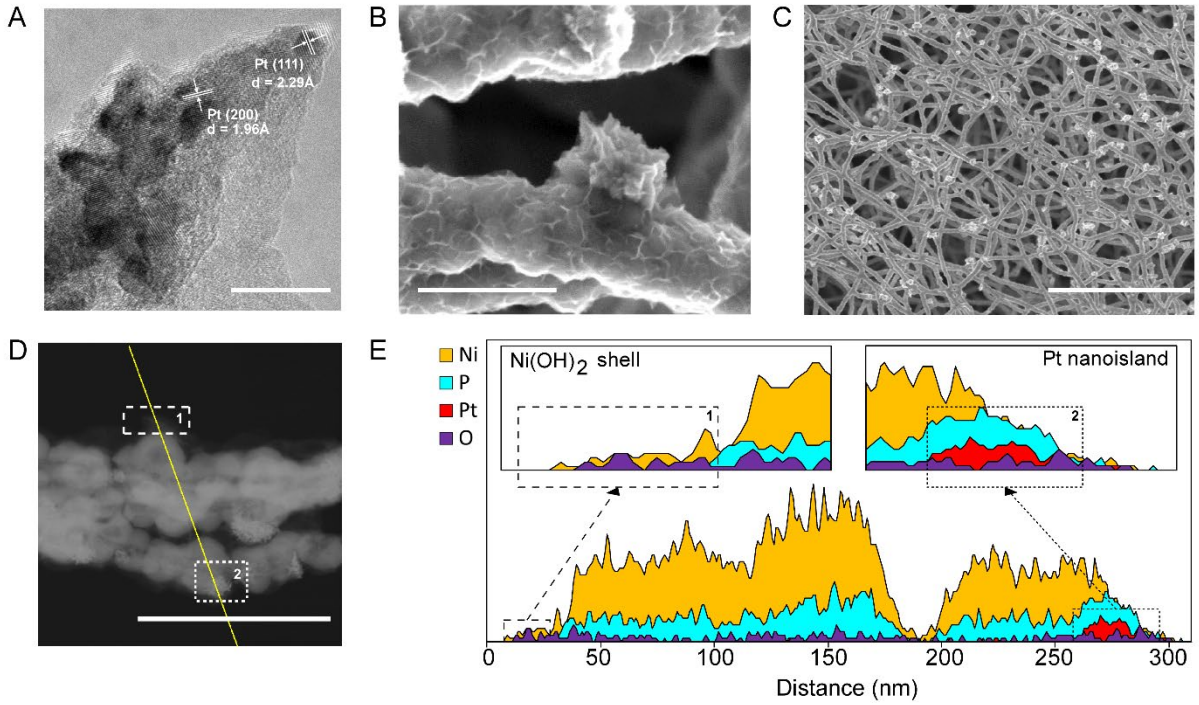

Figure 2. (a) HRTEM, (b) high-magnification SEM, (c) low-magnification SEM, and (d) HAADF-STEM images of a Pt–$Ni(OH)_2$ nanonetwork with 35.5 $\mu g_{Pt}\,cm^{-2}_{geo}$. (e) EDX line scan identifying the (1) $Ni(OH)_2$ shell and (2) platinum nanoisland. Scale bars are 5 nm, 200 nm, 5 µm, and 200 nm for (a), (b), (c), and (d), respectively.

The concentration of Na_2PtCl_6 in the platinum deposition bath was used to control the final loading of platinum in the Pt–$Ni(OH)_2$ nanonetworks. The overall platinum loading, measured using inductively couple plasma optical emission spectroscopy (ICP–OES), ranged from 2.50 µg to 46.4 µg or 1.39 wt% to 19.1 wt% (**Figure S1e**). Nickel is oxidized under ambient conditions upon exposure to dissolved oxygen in water [35,36]. An oxide layer less than 10 nm thick spontaneously grew around the as-deposited nickel, shown in **Figure 2b**, yielding $Ni(OH)_2$-coated nanonetworks. High angle annular dark-field scanning TEM (HAADF–STEM) and energy-dispersive X-ray spectroscopy (EDX) were performed to corroborate the composition of the Ni–P core, $Ni(OH)_2$ outer layer, and platinum nanoislands (**Figure 2d–e**). The lack of platinum and phosphorus in the outer shell of the nanonetworks, as well as the positive identification of platinum in the nanoisland, support our hypothesized structure. Further EDX mapping (**Figure S2**) provided additional confirmation of the composition of the platinum nanoislands, as well as the oxygen-rich surface layer. The lack of phosphorus in both the $Ni(OH)_2$ surface layer and the platinum nanoislands

also suggests that it does not affect the electronic structure of the surface material. Therefore, we do not expect phosphorus to play an important role in the electrocatalytic performance of the Pt–$Ni(OH)_2$ nanonetworks.

Two additional controls were created to help elucidate the contributions of both the Pt–$Ni(OH)_2$ material system and the phage-templated structure while testing electrocatalytic behavior (see Supplementary Infromation). First, platinum was electrolessly deposited directly onto the phage scaffold, yielding nanonetworks with wire diameters around 150 nm and an average loading of 140 ± 24 μg_{Pt}, measured with ICP–OES. (**Figure S3**). The Pt nanonetworks offer a useful comparison to the Pt–$Ni(OH)_2$ nanonetworks because they are characterized by an analogous nanostructure and similar geometric areas. This allows for a closer comparison than that between the Pt–$Ni(OH)_2$ nanonetworks and any similar platinum-based systems in the literature. The Pt nanonetworks can also demonstrate the HER performance associated with high platinum loading in the catalyst, but without cooperativity between Pt and $Ni(OH)_2$. As a second control, a similar Pt–$Ni(OH)_2$ synthesis procedure was applied directly on a titanium foil substrate, without the phage hydrogel. This untemplated version of the Pt–$Ni(OH)_2$ material system possessed a similar morphology to the phage-templated nanonetworks, including platinum nanoislands on agglomerated Ni–P nanoparticles and an oxidized surface layer (**Figure S4**).

The crystallography of the Pt–$Ni(OH)_2$ nanonetworks was characterized using X-ray diffraction (XRD) on samples at several different platinum loadings and compared to as-deposited nickel wires. The Ni–P alloy deposit was largely amorphous, displaying only a weak, broad peak centered on the (111) facet of fcc nickel (ICDD reference pattern 04–010–6148), similar to previous literature reports for high-phosphorus-content, electroless nickel deposits [37]. Additionally, this provides strong evidence against the formation of metal phosphides like Ni_3P, which have also shown electrocatalytic HER activity [38]. In contrast, the deposited platinum nanoislands were crystalline in nature, as seen by the appearance of fcc platinum (ICDD reference pattern 04–001–0112) with higher platinum loadings (**Figure 3a**). These facets were corroborated using high-resolution TEM (HRTEM), shown in **Figure 2a**. Lattice spacings of 1.96 Å and 2.29 Å were measured, corresponding to the (200) and (111) planes, respectively, of platinum. The

outer, oxidized nickel layer was too thin to deliver an identifiable signal with XRD and appeared largely amorphous under the TEM beam.

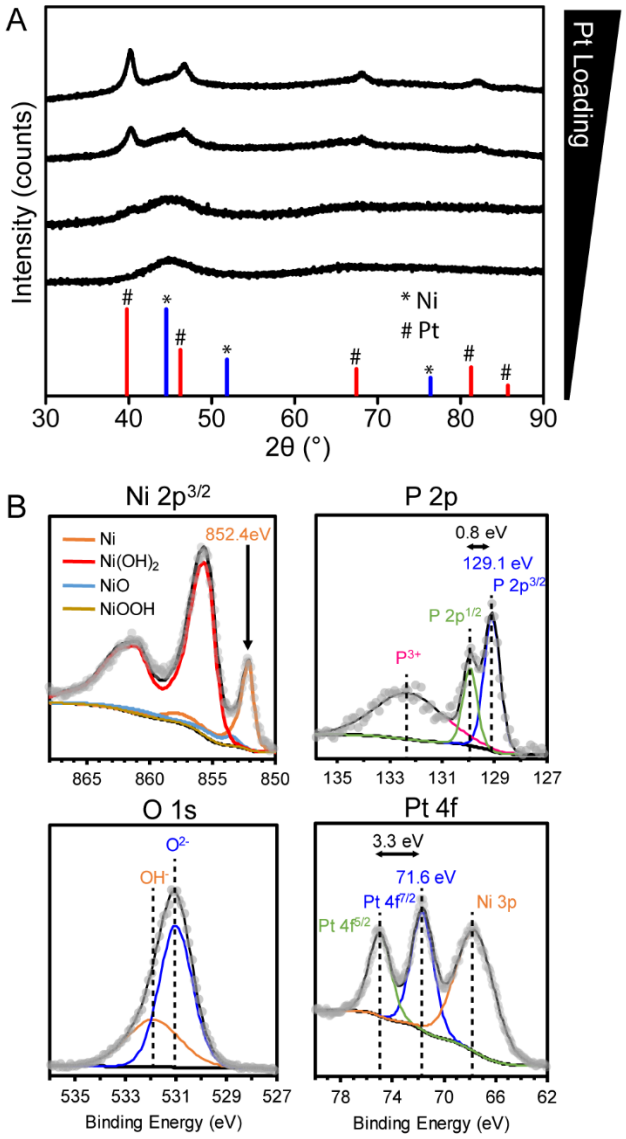

Figure 3. (a) XRD characterization at four different platinum loadings (0, 35.5, 59.2, and 90.1 μg_{Pt} cm^{-2}_{geo}, respectively) and (b) XPS characterization of Pt–$Ni(OH)_2$ nanonetworks in the Ni $2p^{3/2}$, P 2p, O 1s, and Pt 4f–Ni 3p regions.

The surface chemistry of the Pt–$Ni(OH)_2$ nanonetworks was characterized with X-ray photoelectron spectroscopy (XPS) and is summarized in **Figure 3b**. The O 1s peak position at a binding energy of 531 eV suggests the formation of $Ni(OH)_2$ as opposed to NiO. Further, the Ni $2p^{3/2}$ spectra confirms the

presence of both metallic Ni^0 and oxidized Ni^{2+} and was deconvolved to Ni, NiO, $Ni(OH)_2$, and NiOOH contributions (see supporting materials). The molar proportions of each nickel species were found to be 16.7%, 5.1%, 77.8%, and 0.1% before the deposition of platinum nanoislands and 14.4%, 1.9%, 83.7%, and 0.0% after the deposition of platinum nanoislands. Thus, $Ni(OH)_2$ is the dominant species in the oxidized surface layer both before and after the platinum deposition process. The P 2p peaks confirm the presence of atomic phosphorus (P $2p^{3/2}$ at 129.1 eV and P $2p^{1/2}$ at 129.9 eV), as well as oxidized P^{3+} species at 132.3 eV. Finally, the Pt $4f^{7/2}$ and $4f^{5/2}$ peaks at 71.6 eV and 71.9 eV, respectively, confirm the zero-valent state of metallic platinum in the deposited nanoislands. **Figure S5** displays the Pt 4f and Ni 3p regions for several platinum synthesis conditions. The molar ratio of Pt:Ni on the surface varies from 0.036 to 0.13 by varying the concentration of $[PtCl_6]^{2-}$ used in the deposition bath, demonstrating that changing the platinum loading directly affects the relative surface concentrations of Pt and $Ni(OH)_2$ and therefore the concentration of available, electrocatalytically active surface sites.

In order to further study the availability of these electrocatalytically active surface sites, the total BET surface area of phage-templated Pt–$Ni(OH)_2$ samples with increasing platinum loadings (0, 1.5, 7.3, and 19 wt% Pt) were determined using Krypton (Kr) adsorption. Kr is preferred to traditional N_2 or Ar as it provides more accurate measurements for small sample sizes. The detailed description of the technique and the calibration method used are discussed in **Section S1.6** and **Figure S6a** in the supplementary materials. Interestingly, the total BET surface area per gram of sample (ranging from 8.5 to 12.7 $m^2\ g^{-1}$) shows a non-monotonic behavior while increasing the platinum content with an optimum at 7.3 wt% Pt (**Figure S7a**). Above this optimal platinum loading, the surface area per gram of sample decreases indicating a lower availability of adsorption sites for Kr molecules. This is further explained by SEM images of these four phage-templated Pt–$Ni(OH)_2$ nanonetworks that shows a gradual increase in the average size of the platinum nanoislands with the platinum concentration (**Figure S7b–e**), ultimately leading to an optimal number of accessible electrocatalytically active platinum adsorption sites per unit mass of sample at 7.3 wt% Pt.

3.2. Electrocatalytic Results

Next, the Pt–$Ni(OH)_2$ nanonetworks were assessed and optimized for their electrocatalytic performance. HER activity was averaged for 3–4 samples at several platinum deposition conditions and is reported here with error bars representing one standard deviation. The exact platinum loading was determined for each sample with ICP–OES after testing. All sample types are denoted by the legend in **Figure 4a**. The phage-templated Pt–$Ni(OH)_2$ nanonetworks were highly active in terms of current density (**Figure 4b**). As expected, samples with the highest platinum loading, 141 ± 6 μg_{Pt} cm^{-2}_{geo}, passed the highest current densities of –250 mA cm^{-2}_{geo} at –70 mV vs. RHE. At higher overpotentials, around 200 mV, these samples reached over –1 A cm^{-2}_{geo}, well above the typical operating current densities for commercial alkaline water electrolyzers [39]. Compared to other reported Pt–$Ni(OH)_2$ electrocatalysts with similar platinum loading, these current densities are nearly an order of magnitude higher, likely due to the increased number of accessible active sites made possible with phage-templating (**Table S1**). Further, Pt–$Ni(OH)_2$ nanonetworks with an average platinum loading as low as 40.8 ± 10.4 μg_{Pt} cm^{-2}_{geo} displayed higher current densities than Pt nanonetworks with an average platinum loading of 566 ± 68 μg_{Pt} cm^{-2}_{geo}. The higher performance of Pt–$Ni(OH)_2$ nanonetworks relative to both Ni nanonetworks and Pt nanonetworks gives evidence of the cooperativity between the individual constituents of the combined material system. This aligns well with other reported Pt–$Ni(OH)_2$ HER electrocatalysts [18,20,22].

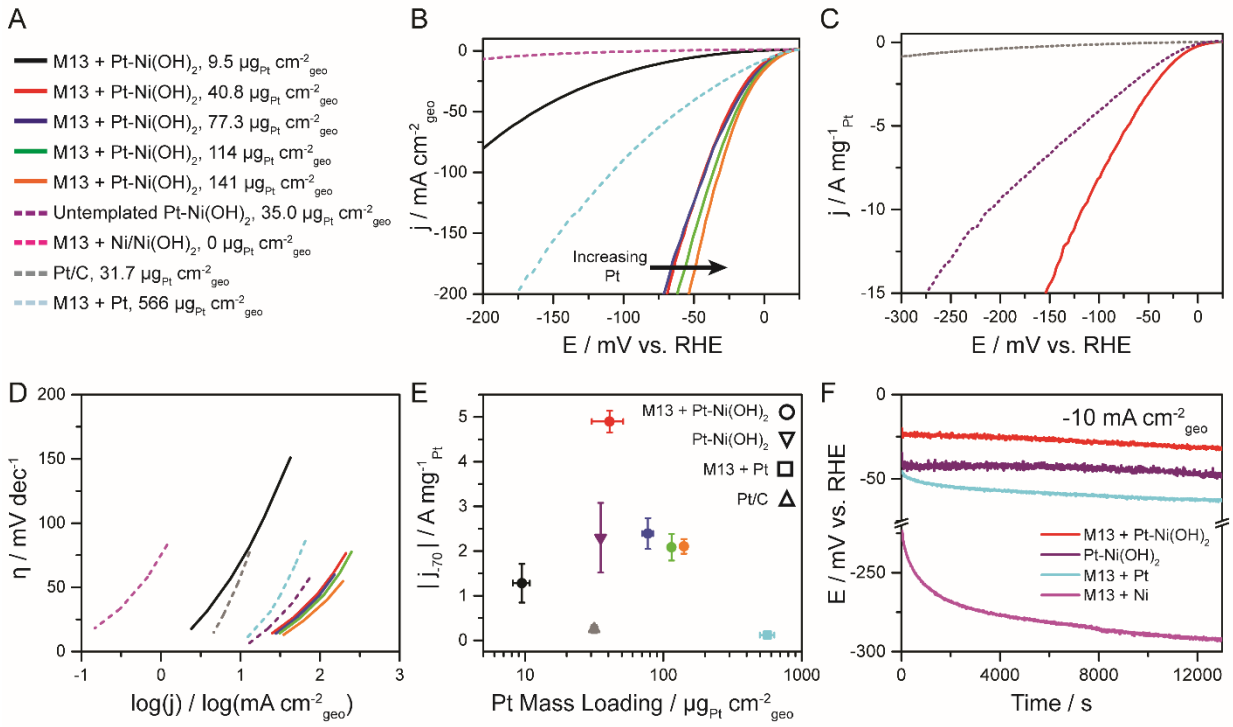

Figure 4. (a) legend entries for tested samples in (b)–(d) and (f); (b) CV scans at comparing Ni and Pt nanonetworks with Pt–$Ni(OH)_2$ nanonetworks at several platinum loadings; (c) mass-normalized CV scans comparing Pt–$Ni(OH)_2$ nanonetworks to Pt/C and untemplated Pt–$Ni(OH)_2$ controls; (d) Tafel plots at several platinum loadings; (e) mass activity benchmarks at –70 mV vs. RHE; (f) galvanostatic stability of Pt–$Ni(OH)_2$ nanonetworks with the optimal platinum loading versus untemplated Pt–$Ni(OH)_2$, Pt nanonetwork, and Ni nanonetwork controls at a current density of –10 mA cm^{-2}_{geo}.

To evaluate mass activities, we compared the phage-templated Pt–$Ni(OH)_2$ nanonetworks to Pt/C and untemplated Pt–$Ni(OH)_2$ controls with similar platinum loadings (**Figure 4c**). Phage-templated Pt–$Ni(OH)_2$ displayed exceptionally strong performance relative to both of these controls. The mass activities of all platinum-containing samples were further compared at a 70 mV overpotential (**Figure 4e**). Although higher platinum loadings in the Pt–$Ni(OH)_2$ nanonetworks increased the achievable current densities, the higher performance corresponded to lower mass activities and thus increasingly inefficient utilization of platinum, in agreement with the relationship between platinum loading and the number of accessible platinum sites per unit mass determined using Kr adsorption (**Figure S7a**). Compared to untemplated Pt–$Ni(OH)_2$, the phage-templated system with the optimal platinum loading demonstrated

2.1 times higher mass activity, further evidence that templating with phage led to improvements in electrocatalytic activity. This improvement may be attributed to improved platinum dispersion on a higher surface area $Ni(OH)_2$ framework, as well as material and morphological changes inherent to material growth on a protein-based surface. Phage-templated Pt–$Ni(OH)_2$ nanonetworks demonstrated nearly an order of magnitude improvement in mass activity relative to Pt/C and phage-templated Pt nanonetworks.

The optimal platinum loading of the Pt–$Ni(OH)_2$ nanonetworks was 40.8 ± 10.4 $\mu g_{Pt}\ cm^{-2}_{geo}$, which corresponded to mass activities of –4.9 ± 0.2 A mg^{-1}_{Pt}. To the best of our knowledge, this is the highest-reported platinum mass activity to date in 1 M KOH (**Table S1**), with no electrocatalyst passing greater than 3 A mg^{-1}_{Pt} under similar testing conditions. An excellent per-site turnover frequency (TOF) of 13 $H_2\ s^{-1}$ was estimated from the Kr adsorption measurements and geometric approximations (see Section S1.10 in the supplementary materials). While the majority of reported Pt–$Ni(OH)_2$ electrocatalysts do not include a TOF estimate, Pt–$Ni(OH)_2$ nanonetworks are around an order of magnitude more active than carbon-supported noble metals tested in similar conditions [40]. Thus, the current density, mass activity, and TOF benchmarked at –70 mV vs. RHE indicate Pt–$Ni(OH)_2$ nanonetworks are highly active, alkaline HER electrocatalysts.

To probe the electrolyte concentration dependency of this high activity, a Pt–$Ni(OH)_2$ nanonetwork sample within the optimal range of platinum loading (34.3 $\mu g_{Pt}\ cm^{-2}_{geo}$) was tested in 0.1 and 1 M KOH (**Figure S9**). In 0.1 M KOH, the sample passed –32 mA cm^{-2}_{geo} and –0.643 A mg^{-1}_{Pt} at an applied potential of –70 mV vs. RHE, compared to –173 mA cm^{-2}_{geo} and –5.09 A mg^{-1}_{Pt} in 1 M KOH. The large discrepancy in activity suggests that cooperativity between Pt and $Ni(OH)_2$ may be enhanced in more concentrated KOH. Interestingly, this diverges with other reported Pt–$Ni(OH)_2$ systems, which display a decrease in HER activity from 0.1 M to 1 M KOH [19]. Most commercial alkaline electrolyzers operate under this highly alkaline regime due to improved OER efficiency; thus, this pH-dependency may be beneficial for commercial integration compared to other electrocatalysts.

As shown in **Figure 4d**, the Tafel slopes of the electrocatalysts were dependent upon the platinum loading of the electrode and fall in drastically different ranges of current density. All Tafel slopes and

exchange current densities can be found in **Table 1**. In the same overpotential regime, biotemplated Ni nanonetworks with zero platinum loading were characterized by a Tafel slope of 70.8 ± 2.1 mV dec^{-1}. Unexpectedly, as the platinum loading increased among biotemplated Pt–$Ni(OH)_2$ samples, the Tafel slope decreased sharply from 88.6 ± 7.9 mV dec^{-1} to values around 60 mV dec^{-1}. The samples with the optimal platinum loading exhibited 60 mV dec^{-1}. This change in Tafel slope may be indicative of a change in the HER rate-limiting step (see Section S1.11 in the supplementary materials) or, more simply, higher mass transfer limitations of intermediates to the active sites at the lowest platinum loading (9.5 ± 1.3 $\mu g_{Pt}\,cm^{-2}_{geo}$). However, definitive HER mechanistic analysis should be relegated to systems that are more well-defined from a morphological and transport perspective. In all cases, the Pt–$Ni(OH)_2$ catalysts proved to be more efficient than the Pt nanonetworks, which featured Tafel slopes of 90.0 ± 3.0 mV dec^{-1}. Both exchange current density and exchange mass current density feature similar trends as the activity measured at a 70 mV overpotential (**Figure S8**). The highest mass exchange current densities were observed for the samples with the optimal platinum loading, giving further evidence that the optimized Pt–$Ni(OH)_2$ nanonetworks are the most intrinsically active as well.

Table 1. Tafel analysis parameters. Tafel slope, exchange current density (j_0) and mass exchange current density for commercial Pt/C, untemplated Pt–$Ni(OH)_2$, Pt nanonetworks, Ni nanonetworks, and Pt–$Ni(OH)_2$ nanonetworks.

Sample	Pt Loading ($\mu g_{Pt}\,cm^{-2}_{geo}$)	Tafel Slope (mV dec^{-1})	j_0 (mA cm^{-2}_{geo})	j_0 (A mg^{-1}_{Pt})
Pt/C	31.7 ± 1.7	140 ± 3	3.1 ± 0.9	0.095 ± 0.023
Untemplated Pt–$Ni(OH)_2$	35.0 ± 0.5	65.6 ± 3.0	11.1 ± 2.5	0.32 ± 0.07
Pt nanonetworks	566 ± 68	90.0 ± 3.0	9.7 ± 1.2	0.017 ± 0.001
Ni nanonetworks	–	70.8 ± 2.1	0.092 ± 0.009	–
Pt–$Ni(OH)_2$ nanonetworks	9.5 ± 1.3	88.6 ± 7.9	1.6 ± 0.6	0.17 ± 0.04
	40.8 ± 10.4	60.7 ± 1.4	15.9 ± 3.4	0.39 ± 0.04
	77.3 ± 6.9	61.9 ± 1.8	17.9 ± 1.9	0.22 ± 0.02
	114 ± 3	61.8 ± 0.8	19.7 ± 0.4	0.17 ± 0.00
	141 ± 6	55.8 ± 4.4	21.8 ± 3.7	0.15 ± 0.03

The Pt–$Ni(OH)_2$ nanonetworks maintained good electrocatalytic stability under both potentiostatic and galvanostatic testing in 1 M KOH. Biotemplated nanonetworks maintained greater than 60% of their

initial current density over eight hours of operation at an overpotential of 70 mV (**Figure S10**). Untemplated Pt–$Ni(OH)_2$ and Pt nanonetworks, on the other hand, demonstrated poor stability under the same overpotential, losing roughly 80% of their initial activity. Ni nanonetworks were not sufficiently active to test under these conditions. Under galvanostatic operation, the biotemplated Pt–$Ni(OH)_2$ nanonetworks displayed less than a 10 mV increase in overpotential after four hours of passing a current density of –10 mA cm^{-2}_{geo} (**Figure 4f**). Untemplated Pt–$Ni(OH)_2$ and Pt nanonetworks featured similar stability, while Ni nanonetworks showed a 60 mV increase under the same testing conditions. It is worth noting that the overpotential required to reach –10 mA cm^{-2}_{geo}, considered the benchmark current density for HER [9], was between 25 and 35 mV for Pt–$Ni(OH)_2$ nanonetworks with the optimal loading. These are among the best reported numbers in alkaline electrolyte [16]. These results give evidence toward the strong stability of the Pt–$Ni(OH)_2$ nanonetworks in terms of both active material and templated structure. Finally, the product composition of the Pt–$Ni(OH)_2$ nanonetworks throughout four hours of operation at –10 mA cm^{-2}_{geo} was measured by in-line gas chromatography to assess the faradaic efficiency (FE) of the reaction. FE values ranging from 98.1% to 101% were calculated, indicating pure H_2 is produced within instrumental precision (see Section S1.9 for details of FE calculations).

The nanonetworks did not exhibit noticeable crystallographic changes, as evidenced by post-stability-testing XRD scans (**Figure S11a**). XPS revealed a greater proportion of $Ni(OH)_2$ (> 90%) in the oxidized surface layer of the Pt–$Ni(OH)_2$ nanonetworks (**Figure S11b**). Although there were no visual signs of large-scale physical destruction to the samples, the oxidized surface layer was visually thicker in SEM and TEM images of post-stability samples (**Figure S12**). Neither result measures the oxidation layer thickness under *in situ* conditions; however, the XPS and imaging results suggest that changes in the oxidation layer structure or composition, which could affect the nature or availability of active sites, may be responsible for the degradation in HER activity.

4. Conclusion

In summary, we present novel, biotemplated HER electrocatalysts synthesized by capitalizing on the natural advantages of M13 bacteriophage, including nanoscopic proportions and genetically engineered binding to metal cations. We applied phage to the bimetallic Pt–$Ni(OH)_2$ material system, yielding contiguous, binder-free Pt–$Ni(OH)_2$ nanonetworks synthesized under ambient conditions. With the optimal platinum loading, the Pt–$Ni(OH)_2$ nanonetworks are highly active, reaching current densities over –1 A cm^{-2}_{geo} under reasonable overpotentials and the highest-reported mass activity to date in 1 M KOH, –4.9 A mg^{-1}_{Pt} at –70 mV vs. RHE. As such, these findings suggest that biotemplated electrode architectures offer a universal and reproducible scaffold for electrocatalyst development *via* extension to other material systems and reactions in electrochemical energy conversion.

Acknowledgement

Funding for this work was provided by the U.S. Defense Advanced Research Project Agency's Living Foundries program award number HR0011-15-C-0084 and by Shell International Exploration & Production, Inc.'s Electrochemical Catalysis & Light-driven Chemical Production award number PO4550155123. NC would like to thank Total S.A. for their support. This work made use of the MRSEC Shared Experimental Facilities supported by the National Science Foundation under award number DMR–1419807. We thank Dr. Charles Settens at the Center for Materials Science and Engineering (CMSE) at MIT for his assistance with XRD, Dr. Elizabeth Shaw at the CMSE at MIT for her assistance with XPS, and Dr. Dong Soo Yun at the Koch Institute for Integrative Cancer Research at MIT for his assistance with HRTEM and HAADF–STEM–EDX.

Supporting Information

Further analysis and characterization can be found in the supplementary materials, including additional synthesis and testing methodology, calculation of TOF, Tafel analysis, compositional characterization of biotemplated scaffolds, EDX mapping, XPS surface characterization as a function of platinum synthesis

conditions, Kr adsorption calibration and testing, post-HER testing images and characterization, additional testing data, and an abbreviated comparison to similar systems reported in the literature.

Notes

The authors declare no competing financial interests.

References

[1] M.S. Dresselhaus, I.L. Thomas, Alternative energy technologies, Nature. 414 (2001) 332–337.

[2] S. Gu, B. Xu, Y. Yan, Electrochemical Energy Engineering: A New Frontier of Chemical Engineering Innovation, Annu. Rev. Chem. Biomol. Eng. 5 (2014) 429–454. doi:10.1146/annurev-chembioeng-060713-040114.

[3] N.S. Lewis, D.G. Nocera, Powering the planet: chemical challenges in solar energy utilization., Proc. Natl. Acad. Sci. U. S. A. 103 (2006) 15729–35. doi:10.1073/pnas.0603395103.

[4] S.Y. Tee, K.Y. Win, W.S. Teo, L.-D. Koh, S. Liu, C.P. Teng, M.-Y. Han, Recent Progress in Energy-Driven Water Splitting, Adv. Sci. 4 (2017) 1600337. doi:10.1002/advs.201600337.

[5] P.C.K. Vesborg, B. Seger, I. Chorkendorff, Recent development in hydrogen evolution reaction catalysts and their practical implementation, J. Phys. Chem. Lett. 6 (2015) 951–957. doi:10.1021/acs.jpclett.5b00306.

[6] O. Schmidt, A. Gambhir, I. Staffell, A. Hawkes, J. Nelson, S. Few, Future cost and performance of water electrolysis: An expert elicitation study, Int. J. Hydrogen Energy. 42 (2017) 30470–30492. doi:10.1016/J.IJHYDENE.2017.10.045.

[7] K. Zeng, D. Zhang, Recent progress in alkaline water electrolysis for hydrogen production and applications, Prog. Energy Combust. Sci. 36 (2010) 307–326. doi:10.1016/J.PECS.2009.11.002.

[8] C.C.L. McCrory, S. Jung, J.C. Peters, T.F. Jaramillo, Benchmarking Heterogeneous Electrocatalysts for the Oxygen Evolution Reaction, J. Am. Chem. Soc. 135 (2013) 16977–16987. doi:10.1021/ja407115p.

[9] C.C.L. Mccrory, S. Jung, I.M. Ferrer, S.M. Chatman, J.C. Peters, T.F. Jaramillo, Benchmarking Hydrogen Evolving Reaction and Oxygen Evolving Reaction Electrocatalysts for Solar Water Splitting Devices, J. Am. Chem. Soc. 137 (2015) 4347–4357. doi:10.1021/ja510442p.

[10] M. Zeng, Y. Li, Recent advances in heterogeneous electrocatalysts for the hydrogen evolution reaction, J. Mater. Chem. A. 3 (2015) 14942–14962. doi:10.1039/C5TA02974K.

[11] P. Xiao, W. Chen, X. Wang, A Review of Phosphide-Based Materials for Electrocatalytic Hydrogen Evolution, Adv. Energy Mater. 5 (2015) 1500985. doi:10.1002/aenm.201500985.

[12] S. Anantharaj, S.R. Ede, K. Sakthikumar, K. Karthick, S. Mishra, S. Kundu, Recent Trends and Perspectives in Electrochemical Water Splitting with an Emphasis on Sulfide, Selenide, and Phosphide Catalysts of Fe, Co, and Ni: A Review, ACS Catal. 6 (2016) 8069–8097. doi:10.1021/acscatal.6b02479.

[13] S. Carenco, D. Portehault, C. Boissière, N. Mézailles, C. Sanchez, Nanoscaled metal borides and phosphides: Recent developments and perspectives, Chem. Rev. 113 (2013) 7981–8065. doi:10.1021/cr400020d.

[14] Y. Jiao, Y. Zheng, M. Jaroniec, S.Z. Qiao, Design of electrocatalysts for oxygen- and hydrogen-involving energy conversion reactions, Chem. Soc. Rev. 44 (2015) 2060–2086. doi:10.1039/C4CS00470A.

[15] N.M. Marković, S.T. Sarraf, H.A. Gasteiger, P.N. Ross, Hydrogen electrochemistry on platinum

low-index single-crystal surfaces in alkaline solution, J. Chem. Soc., Faraday Trans. 92 (1996) 3719–3725. doi:10.1039/FT9969203719.
[16] N. Mahmood, Y. Yao, J.-W. Zhang, L. Pan, X. Zhang, J.-J. Zou, Electrocatalysts for Hydrogen Evolution in Alkaline Electrolytes: Mechanisms, Challenges, and Prospective Solutions, Adv. Sci. 5 (2018) 1700464. doi:10.1002/advs.201700464.
[17] R. Subbaraman, D. Tripkovic, K.-C. Chang, D. Strmcnik, A.P. Paulikas, P. Hirunsit, M. Chan, J. Greeley, V. Stamenkovic, N.M. Markovic, Trends in activity for the water electrolyser reactions on 3d M(Ni,Co,Fe,Mn) hydr(oxy)oxide catalysts, Nat. Mater. 11 (2012) 550–557. doi:10.1038/nmat3313.
[18] R. Subbaraman, D. Tripkovic, D. Strmcnik, K.-C. Chang, M. Uchimura, a P. Paulikas, V. Stamenkovic, N.M. Markovic, Enhancing Hydrogen Evolution Activity in Water Splitting by Tailoring Li+-Ni(OH)2-Pt Interfaces, Science. 334 (2011) 1256–1260. doi:10.1126/science.1211934.
[19] H. Yin, S. Zhao, K. Zhao, A. Muqsit, H. Tang, L. Chang, H. Zhao, Y. Gao, Z. Tang, Ultrathin platinum nanowires grown on single-layered nickel hydroxide with high hydrogen evolution activity, Nat. Commun. 6 (2015) 6430. doi:10.1038/ncomms7430.
[20] X. Yu, J. Zhao, L.-R. Zheng, Y. Tong, M. Zhang, G. Xu, C. Li, J. Ma, G. Shi, Hydrogen Evolution Reaction in Alkaline Media: Alpha- or Beta-Nickel Hydroxide on the Surface of Platinum?, ACS Energy Lett. 3 (2018) 237–244. doi:10.1021/acsenergylett.7b01103.
[21] Y. Wang, L. Chen, X. Yu, Y. Wang, G. Zheng, Superb Alkaline Hydrogen Evolution and Simultaneous Electricity Generation by Pt-Decorated Ni3N Nanosheets, Adv. Energy Mater. 7 (2017) 1601390. doi:10.1002/aenm.201601390.
[22] L. Wang, Y. Zhu, Z. Zeng, C. Lin, M. Giroux, L. Jiang, Y. Han, J. Greeley, C. Wang, J. Jin, Platinum-nickel hydroxide nanocomposites for electrocatalytic reduction of water, Nano Energy. 31 (2017) 456–461. doi:10.1016/J.NANOEN.2016.11.048.
[23] J.R. McKone, B.F. Sadtler, C.A. Werlang, N.S. Lewis, H.B. Gray, Ni–Mo Nanopowders for Efficient Electrochemical Hydrogen Evolution, ACS Catal. 3 (2013) 166–169. doi:10.1021/cs300691m.
[24] M.B. Dickerson, K.H. Sandhage, R.R. Naik, Protein- and Peptide-Directed Syntheses of Inorganic Materials, Chem. Rev. 108 (2008) 4935–4978. doi:10.1021/cr8002328.
[25] J. Qi, X. Dang, P.T. Hammond, A.M. Belcher, Highly Efficient Plasmon-Enhanced Dye-Sensitized Solar Cells through Metal@Oxide Core–Shell Nanostructure, ACS Nano. 5 (2011) 7108–7116. doi:10.1021/nn201808g.
[26] N. Nuraje, X. Dang, J. Qi, M.A. Allen, Y. Lei, A.M. Belcher, Biotemplated synthesis of perovskite nanomaterials for solar energy conversion, Adv. Mater. 24 (2012) 2885–2889. doi:10.1002/adma.201200114.
[27] D. Oh, J. Qi, Y.-C. Lu, Y. Zhang, Y. Shao-Horn, A.M. Belcher, Biologically enhanced cathode design for improved capacity and cycle life for lithium-oxygen batteries., Nat. Commun. 4 (2013) 2756. doi:10.1038/ncomms3756.
[28] K.T. Nam, D.-W. Kim, P.J. Yoo, C.-Y. Chiang, N. Meethong, P.T. Hammond, Y.-M. Chiang, A.M. Belcher, Virus-Enabled Synthesis and Assembly of Nanowires for Lithium Ion Battery Electrodes, Science. 312 (2006) 885–888. doi:10.1126/science.1122716.
[29] D. Oh, J. Qi, B. Han, G. Zhang, T.J. Carney, J. Ohmura, Y. Zhang, Y. Shao-Horn, A.M. Belcher, M13 virus-directed synthesis of nanostructured metal oxides for lithium-oxygen batteries, Nano Lett. 14 (2014) 4837–4845. doi:10.1021/nl502078m.
[30] B.Y. Lee, J. Zhang, C. Zueger, W.J. Chung, S.Y. Yoo, E. Wang, J. Meyer, R. Ramesh, S.W. Lee, Virus-based piezoelectric energy generation, Nat Nanotechnol. 7 (2012) 351–356. doi:10.1038/nnano.2012.69.
[31] N.M.D. Courchesne, M.T. Klug, P.Y. Chen, S.E. Kooi, D.S. Yun, N. Hong, N.X. Fang, A.M. Belcher, P.T. Hammond, Assembly of a bacteriophage-based template for the organization of materials into nanoporous networks, Adv. Mater. 26 (2014) 3398–3404.

doi:10.1002/adma.201305928.
[32] S.M. Alia, S. Pylypenko, K.C. Neyerlin, S.S. Kocha, B.S. Pivovar, Nickel Nanowire Oxidation and Its Effect on Platinum Galvanic Displacement and Methanol Oxidation, ECS Trans. 64 (2014) 89–95. doi:10.1149/06403.0089ecst.
[33] G.O. Mallory, The Fundamental Aspects of Electroless Nickel Plating, in: G.O. Mallory, J.B. Hajdu (Eds.), Electroless Plat. Fundam. Appl., William Andrew Publishing/Noyes, 1990: p. 5.
[34] E. De Robertis, L.M. Abrantes, A.J. Motheo, The influence of experimental parameters on the structure, morphology and electrochemical behavior of Pd–P thin films prepared by electroless deposition, Thin Solid Films. 516 (2008) 6266–6276. doi:10.1016/j.tsf.2007.11.121.
[35] D.S. Hall, D.J. Lockwood, C. Bock, B.R. MacDougall, Nickel hydroxides and related materials: a review of their structures, synthesis and properties., Proc. R. Soc. A. 471 (2015) 20140792. doi:10.1098/rspa.2014.0792.
[36] D.S. Hall, C. Bock, B.R. MacDougall, The Electrochemistry of Metallic Nickel: Oxides, Hydroxides, Hydrides and Alkaline Hydrogen Evolution, J. Electrochem. Soc. 160 (2013) F235–F243. doi:10.1149/2.026303jes.
[37] M. Sribalaji, P. Arunkumar, K.S. Babu, A.K. Keshri, Crystallization mechanism and corrosion property of electroless nickel phosphorus coating during intermediate temperature oxidation, Appl. Surf. Sci. 355 (2015) 112–120. doi:10.1016/J.APSUSC.2015.07.061.
[38] A.B. Laursen, R.B. Wexler, M.J. Whitaker, E.J. Izett, K.U.D. Calvinho, S. Hwang, R. Rucker, H. Wang, J. Li, E. Garfunkel, M. Greenblatt, A.M. Rappe, G.C. Dismukes, Climbing the Volcano of Electrocatalytic Activity while Avoiding Catalyst Corrosion: Ni3P, a Hydrogen Evolution Electrocatalyst Stable in Both Acid and Alkali, ACS Catal. 8 (2018) 4408–4419. doi:10.1021/acscatal.7b04466.
[39] L. Bertuccioli, A. Chan, D. Hart, F. Lehner, B. Madden, Eleanor Standen, Study on development of water electrolysis in the EU, Lausanne, Cambridge, 2014.
[40] Y. Zheng, Y. Jiao, Y. Zhu, L.H. Li, Y. Han, Y. Chen, M. Jaroniec, S.-Z. Qiao, High Electrocatalytic Hydrogen Evolution Activity of an Anomalous Ruthenium Catalyst, J. Am. Chem. Soc. 138 (2016) 16174–16181. doi:10.1021/jacs.6b11291.

William C. Records received his B.S. in chemical engineering from Carnegie Mellon University in 2015 and M.S. in chemical engineering practice at the Massachusetts Institute of Technology in 2017. He is currently a Ph.D. candidate in chemical engineering at Massachusetts Institute of Technology, where his research focuses on the development of nanostructured electrocatalysts for renewable energy applications.

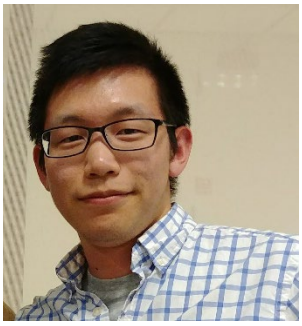

Youngmin Yoon graduated with a B.A. in Chemistry from the University of Pennsylvania in 2011 and a Ph.D. in Chemistry from the Massachusetts Institute of Technology in 2018. His research areas include electrochemistry, materials chemistry, and inorganic chemistry.

Jacqueline F. Ohmura received her bachelor's degree at The Ohio State University in Materials Science and Engineering with a minor in life science in 2011. She received her Biological Engineering PhD at Massachusetts Institute of Technology in 2018 where she is currently a postdoctoral associate. Her research interests include leveraging biological tool sets towards medical and energy challenges.

Nicolas Chanut received his B.S. in chemistry and M.S in catalysis and physical chemistry from Université Claude Bernard Lyon, France and he earned a Ph.D in condensed matter and nanoscience in 2016 from Aix-Marseille Université, France. He is now a postdoctoral associate at Massachusetts Institute of Technology in the joint MIT-CNRS Laboratory 'Multiscale Material Science for Energy and Environment'. His research interests include the development and characterization of porous materials for energy and environmental applications.

Angela M. Belcher is a biological and materials engineer with expertise in the fields of biomaterials, biomolecular materials, organic-inorganic interfaces, and solid-state chemistry and devices. Her primary research focus is evolving new materials for energy, electronics, the environment, and medicine. She received her B.S. in Creative Studies with an emphasis in biology from The University of California, Santa Barbara. She earned a Ph.D. in inorganic chemistry at UCSB in 1997. She joined the faculty at MIT in 2002. Some recent awards include 2018 National Academy of Engineers Fellow, 2015 National Academy of Inventors Fellow, and the 2013 Lemelson-MIT Prize.